Original Full Length Article

Ultrastructure of regenerated bone mineral surrounding hydroxyapatite–alginate composite and sintered hydroxyapatite

Andre L. Rossi [a], Isabela C. Barreto [b], William Q. Maciel [a], Fabiana P. Rosa [b], Maria H. Rocha-Leão [c], Jacques Werckmann [a], Alexandre M. Rossi [d], Radovan Borojevic [a], Marcos Farina [a,*]

[a] Institute of Biomedical Sciences, Federal University of Rio de Janeiro (UFRJ), Brazil
[b] Institute of Health Sciences, Federal University of Bahia, Brazil
[c] School of Chemistry, UFRJ, Brazil
[d] Brazilian Center for Physics Research, CBPF, Brazil

ARTICLE INFO

ABSTRACT

We report the ultrastructure of regenerated bone surrounding two types of biomaterials: hydroxyapatite–alginate composite and sintered hydroxyapatite. Critical defects in the calvaria of Wistar rats were filled with micrometer-sized spherical biomaterials and analyzed after 90 and 120 days of implantation by high-resolution transmission electron microscopy and Fourier transform infrared attenuated total reflectance microscopy, respectively. Infrared spectroscopy showed that hydroxyapatite of both biomaterials became more disordered after implantation in the rat calvaria, indicating that the biological environment induced modifications in biomaterials structure. We observed that the regenerated bone surrounding both biomaterials had a lamellar structure with type I collagen fibers alternating in adjacent lamella with angles of approximately 90°. In each lamella, plate-like apatite crystals were aligned in the c-axis direction, although a rotation around the c-axis could be present. Bone plate-like crystal dimensions were similar in regenerated bone around biomaterials and pre-existing bone in the rat calvaria. No epitaxial growth was observed around any of the biomaterials. A distinct mineralized layer was observed between new bone and hydroxyapatite–alginate biomaterial. This region presented a particular ultrastructure with crystallites smaller than those of the bulk of the biomaterial, and was possibly formed during the synthesis of alginate-containing composite or in the biological environment after implantation. Round nanoparticles were observed in regions of newly formed bone. The findings of this work contribute to a better understanding of the role of hydroxyapatite based biomaterials in bone regeneration processes at the nanoscale.

Introduction

The clinical success of an implant is dependent on the juxtaposition and vitality of the new bone tissue regenerated around the biomaterials as well as on the integrity of the bone–implant interface, which acts as an anchoring surface for the collagen fibers that are formed later [1,2]. Several biomaterials and biocomposites are being used in the field of bone engineering [3–8]. However the behavior of these materials after implantation and the structural characteristics of the newly formed tissue surrounding the materials at the nanoscale, are not completely known. The way new bone is structured and adhered to the surface of the biomaterial and the potential distinct mineralized phases present, should be studied before clinical applications, aiming to the materials optimization. Hydroxyapatite

has been used alone, or in association with cells, growth factors and polymers in a wide range of medical applications because of its biocompatibility, bioactivity and osteoconduction properties [2,3,9].

The association of hydroxyapatite with alginate is a promising composite, widely applied in biomedical engineering to form porous mineralized scaffolds after calcination [10–12]. Alginate is a natural polysaccharide extracted from seaweed and bacteria. The addition of divalent cations, such as calcium, to alginate in aqueous solution may induce cross links between molecules and the formation of hydrogels, a tridimensional network that permanently stabilizes the polymers.

In a previous work [13], we showed that sub-millimeter spheres of non-calcined hydroxyapatite–alginate (HA-Alg) composite used as grafts in critical defects of rat calvaria promoted bone formation in different length scales. The apparent bioactive behavior of the biomaterial could be related to the alginate phase of the composite that forms highly anionic polymers (rich in carboxylates) with a potential to adsorb specific molecules from the extra-cellular matrix and thus induce osteoblast differentiation locally. However, the evolution of

* Corresponding author at: Laboratório de Biomineralização, ICB, CCS, UFRJ, CEP 21941-902, Rio de Janeiro, RJ, Brazil.
E-mail address: mfarina@anato.ufrj.br (M. Farina).

this new composite after several weeks of implantation, the consequences to the bone–biomaterial interface and the ultrastructure of the regenerated bone surrounding HA-Alg had not been evaluated at the nanometer scale [13].

Similar to other mineralized tissues, bone is a hierarchically structured composite. It is formed by apatite crystals and organic components, of which type I collagen represents 90% [14,15]. Depending on the bone type and the species, different arrangements of collagen fibrils and apatite crystals have been reported [16].

Each type of fibril arrangement has mechanical specificities and advantages, which are related to the bone function [16]. Compared to parallel-fibered and radial-fibered arrangements, the plywood model in the osteonal system and lamellar bone is mechanically optimized to support stress from any direction applied [16–18]. Different types of plywood-like structures have been described for bone: orthogonal plywood [19], twisted plywood [19] and rotated plywood [20].

Woven bone is formed by loosely oriented fibers arranged in bundles with little evidence of intra-fibrillar mineralization [21]. Its rate of mineralization is faster than that of lamellar bone. Woven bone is the first bone formed during initial bone formation in fracture and pathologic circumstances [21].

The first mineralized layer formed at the interface bone–biomaterial is a cement layer-like structure, which is analogous to the cement layer in the contour of a new haversian system formed by the remodeling process of bone [1,22]. This layer is free from collagen and presents an organic matrix rich in bone sialoprotein and osteopontin that provides nucleation and modulation sites for calcium phosphate mineralization [1].

Bone mineralization is a cell-regulated process that maintains the morphology and strength of the tissue [23] and involves an organic matrix, specific proteins and a system for transporting ions to the mineralizing site [24]. Different mechanisms for the nucleation of bone crystals have been proposed: (1) osteoblast cells may secrete membrane-bound matrix vesicles (50–200 nm in diameter) into the osteoid tissue by budding. Hydroxyapatite nanocrystals grow inside these vesicles and eventually disrupt the vesicles forming mineralized nodules in the extracellular matrix [23]; (2) organic components from the extracellular matrix may be directly related to nucleation of hydroxyapatite crystals and nodules formation, independently from the matrix vesicles. These structures are known as crystal sheaths or crystal ghosts [25]; (3) mineralization of bone apatite crystals is mediated first by extracellular matrix vesicles and later by type I collagen fibrils, both inside type I collagen fibrils or onto the fibrils independently from the matrix vesicles mineralization process [26,27]. By analyzing the mineralizing leg tendon from the domestic turkey by electron tomography, Landis et al. [28] found that the mineral phase inside gaps of the fibrils was present as small irregularly shaped platelets with the crystallographic c-axes pointing parallel to the collagen long axes.

Understanding the mechanism by which bone regenerates around new composite biomaterials is important for developing and optimizing new biomaterials for bone engineering as well as for understanding the influence of the different biomaterials in bone formation. The architecture of bone, including the morphology, dimensions and distribution of the nanocrystals in the cement layer and collagen fibrils should be investigated in detail to assess their crystallographic characteristics and their role in bone strength and mechanical properties around an implant. Thus, the motivation for this work was to find a possible correlation between nanostructure at the interface biomaterial–newly formed bone, and characteristics of regenerated bone at the meso and macro-scales.

In this work we investigated the mineralized material surrounding HA-Alg composite and sintered hydroxyapatite (HA-Sint) used to regenerate critical bone defects in rat calvaria by high-resolution electron microscopy (HRTEM)/electron diffraction and Fourier transform infrared attenuated total reflectance microscopy (FTIR). Our results revealed differences mainly in the new mineralized regions in close proximity to the implanted biomaterials.

Materials and methods

Biomaterials

Synthetic hydroxyapatite powder was mixed with sodium alginate (Keltone) in a 15:1 proportion. The mixture was dropped from a syringe into a solution of calcium chloride (0.15 mol/L $CaCl_2$) at room temperature to produce a composite of small sub-millimeter-sized spheres containing polymers of calcium alginate mixed with the nanoparticles [13,29]. The spheres were removed from solution and washed in distilled water. Half of the sample was air dried and stored at room temperature (HA-Alg). The dried spheres maintained the same HA/Alginate content and similar dimension than as-prepared spheres. The other half of the sample was calcined in a muffle under oxygen flux at 1100 °C (HA-Sint). The thermal treatment was conducted to: (i) eliminate alginate from the spheres (T > 240 °C) and (ii) induce the sintering of hydroxyapatite particles (T > 800 °C). The sintering process increases the mean particle size, drastically reduces the inter-particle spaces and produces sample densification. In our case, the thermal treatment at 1100 °C produced an efficient densification of HA particles: the mean particle size increased from its non annealed value while the diameters of the spheres decreased.

Spheres containing alginate and sintered hydroxyapatite were sieved to produce samples with diameters ranging from 400 to 600 μm. Before implantation in rats, biomaterials were analyzed by TEM (Transmission Electron Microscopy) and SAED (Select Area Electron Diffraction). The spheres were embedded in epoxy resin, ultrathin sectioned (ca. 70 nm thick) using an ultramicrotome (PT-XL PowerTome, RMC) and analyzed in a JEOL 1200-EX electron microscope. SAED from biomaterials were obtained with constant camera length and an accelerating voltage of 100 kV. TEM imaging and diffraction were previously calibrated with a gold standard (Ted Pella, Inc).

Biomaterial implantation

For microscopy studies we used 12 male rats (*Rattus norvegicus*), 6 rats for each biomaterial, besides the control group. The rats were between 3 and 4 months old, with body weights ranging from 350 to 420 g. Critical circular defects of circa 8 mm in diameter and 1.5 mm deep were made in the calvaria between anterior and posterior cranial sutures using a trephine milling cutter under constant irrigation and were filled with HA-Alg or HA-Sint biomaterials. Anesthesia was given by intramuscular injection of ketamine chloride (0.1 mL/100 g of body mass) and sedation plus analgesia was given by intramuscular injection in a single dose of xylazine chloride (0.04 mL/100 g body mass). After 90 days of implantation, rats were killed with a lethal dose of ketamine chloride and the samples containing the defect were removed from the calvaria. This work was approved by the Ethical Committee on the Use and Care of Animals of the State University of Feira de Santana (Bahia-Brazil). For Fourier transform infrared spectroscopy (FTIR) additional 2 rats were used and analyzed after 120 days.

Sample preparation and light microscopy observations

After 90 days of implantation, samples containing the circular defect in calvaria with a small portion of original bone in the periphery were obtained surgically and sectioned by sagittal planes. Samples were fixed for 48 h in a solution containing glutaraldehyde (2.5%) and paraformaldehyde (4%) in cacodilate buffer (0.1 M, pH 7.3). Post-fixation was performed with osmium (1%) in cacodylate buffer

(0.1 M, pH 7.3) for 1 h in the dark. They were further washed in the buffer, dehydrated in an acetone series (from 30 to 100%) and embedded in epoxy resin (Polybed — Ted Pela Inc.). Resin polymerization was performed at 70 °C for 24 h.

Semi-thin (2 μm) sections of HA-Alg and HA-Sint samples were obtained using an ultramicrotome (PT-XL PowerTome, RMC) with a diamond knife (Ted Pella, Inc.). Samples were sectioned in sagittal planes near the diameter of the circular defect. Observation by light microscopy was performed with a Zeiss (Axioplan) with 10× to 100× objective lenses. Sections were stained with toluidine blue and basic fuchsin. Several sections from different regions of all samples containing the biomaterial and the newly formed bone were analyzed in the bright field, differential interference contrast and polarizing light modes. Histological details from the HA-Alg samples have been published previously [13]. One typical sample from each HA-Alg and HA-Sint containing biomaterial and new bone (Fig. 3A) was selected for further TEM analysis. The same region observed by optical microscopy was investigated by TEM to perform a correlative microscopy study so that the structure could be compared at different length scales. In addition, different regions from the same sample were compared both morphologically and quantitatively.

High-resolution transmission electron microscopy (HRTEM)

Ultra-thin (~70 nm) sections from the same regions observed by light microscopy where the new formed bone was in close contact with the spheres were obtained using an ultramicrotome (PT-XL PowerTome, RMC) and a diamond knife (Ted Pella, Inc.). Five copper grids (lacey formvar/carbon, 400 mesh, Ted Pella, Inc.) with approximately five ultra-thin sections per grid were prepared for TEM analysis. No staining was performed. The sections were analyzed with a Jeol 3010 TEM with a LaB_6 source or a FEI-TITAN 80-300 with a FEG source both operated at 300 kV. The images were digitized with a 1024×1024 CCD camera (Gatan 794SC multiscan digital camera) or a 2000×2000 (Gatan 1000P ultrascan), respectively. Fast fourier transform (FFT) of high-resolution transmission electron microscopy images were obtained and analyzed using Digital Micrograph software (Gatan). Stoichiometric hydroxyapatite crystallizes in the hexagonal crystal system (space group $P6_3/m$) with unit cell parameters: $a \approx b \approx 0.941$ and $c \approx 0.688$ nm. The lattice planes were indexed by comparing the interplanar distances and relative angles in the analyzed crystallites with crystallographic parameters in hydroxyapatite standards (JCPDF, cards No 86-1203 and JEMS — electron microscopy software java version). Selected area electron diffraction (SAED) was performed using a JEOL 1200 EX working at 100 kV or a Jeol 3010 TEM operated at 300 kV. Crystallites were quantified from TEM images. A profile tool from Digital Micrograph software (Gatan) was used to detect edge limits from small contrast variation. Prior to image analysis, a gold sample standard (Ted Pella, Inc.) was used to calibrate the EM magnification using the same software. Crystals were measured individually. The same image processing tool was used to show contrast variation in adjacent lamellae in both light and electron microscopy images (Fig. 3).

Fourier transform infrared spectroscopy

Sections of circa 200 μm-thick of the epoxy-embedded samples containing the new bone formed and the biomaterials spheres were obtained with a low-speed diamond wheel saw (Model 650 — South Bay Technology Inc.) and polished in a silicon carbide sand paper series. Fourier transform infrared attenuated total reflectance microscopy (FTIR) analysis of PO_4 domains between 1150 cm^{-1} and 950 cm^{-1} was performed in sections from HA-Alg and HA-Sint biomaterials before implantation and after 120 days of implantation in the rat calvaria using a Shimadzu IR- Prestige-21/AIM-880 operating in ATR mode and attached to a light microscope with 15× objective lens magnification.

Results

HA-Alg and HA-Sint biomaterials

Ultrathin sections of HA-Alg and HA-Sint spheres were analyzed by TEM before implantation. The HA-Alg nanoparticles were smaller and present in a higher concentration (number of particles per unit volume) in the spheres in comparison with those of HA-Sint. In addition, the morphology of the particles differed. HA-Alg nanoparticles were more elongated than HA-Sint (Figs. 1A and B). This change in particle concentration and particle size may be attributed to sintering effects on HA-Sint spheres caused by thermal treatment at high temperature (1100 °C). SAED patterns of the biomaterials obtained under similar conditions revealed continuous rings for HA-Alg (Fig. 1A, inset), whereas individual spots were seen in the HA-Sint samples (Fig. 1B, inset), showing that the HA-Sint grains were larger and present in a smaller density.

Pre-existing bone

The ultrastruture of the pre-existing bone from a sagittal section near the border of the defect was assessed by TEM and used as a reference for comparison studies with the new bone tissue formed around HA-Alg and HA-Sint. This particular cutting plane allowed for the observation of type I collagen fibrils with their longer axes perpendicular to the electron beam. Collagen fibrils with the characteristic banding pattern were seen oriented in parallel (Fig. 2A). SAED from this region showed a typical dispersion of the (002) planes of apatite crystals around the direction of the longer axes of the fibrils (Fig. 2A, inset). The banded regions were composed of plate-like crystals, which appeared as dark needles (arrow) when observed side-on and as less electron-dense regions with scarcely defined contours (arrowhead) when observed top-on under higher magnification (Fig. 2B). The inset in Fig. 2B shows a lattice image of an individual apatite nanocrystal.
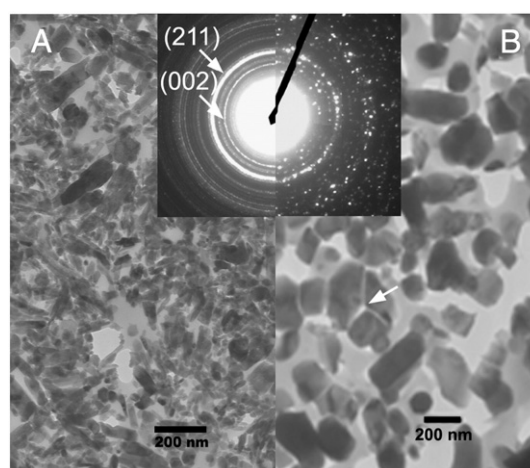

Fig. 1. TEM images and SAED of HA-Alg and HA-Sint biomaterials before implantation in the rat calvaria. (A) HA-Alg. Nanoparticles were smaller, more elongated and in a higher concentration in the spheres when compared with those of HA-Sint. Inset: SAED of HA-Alg. Rings were continuous and homogeneous. The more intense ring corresponding to the (211) planes (0.279 nm) although (112) and (300) planes have similar interplanar distances (0.277 and 0.269 nm, respectively) and also contributed to the final intensity. (B) HA-Sint. The calcination process induced the fusion of nanoparticles in some regions (arrow). Inset: SAED of HA-Sint. Sharp bright spots were observed instead of rings due to the presence of larger and fewer crystals.
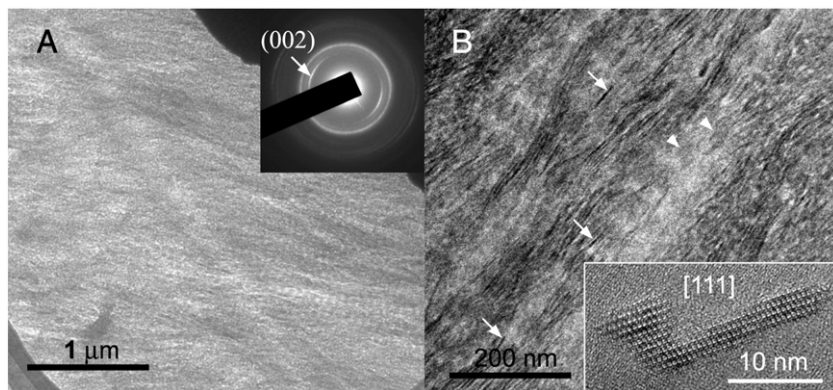
Fig. 2. TEM, HRTEM and SAED of pre-existing cortical bone. (A) Characteristic banding pattern of mineralized collagen fibrils. Inset: SAED composed of (002) incomplete rings (0.34 nm), indicating a dispersed orientation of the *c*-axis direction of apatite crystals. The most intense complete ring corresponds to 0.28 nm. (B) Higher magnification of the collagen-banding pattern from a similar region. Hydroxyapatite plate-like crystals appeared as dark needles (arrow) when observed side-on and as less electron-dense regions with scarcely defined contours (arrow head) when observed top-on. Inset: HRTEM of an apatite nanocrystal observed in the [111] zone axis.
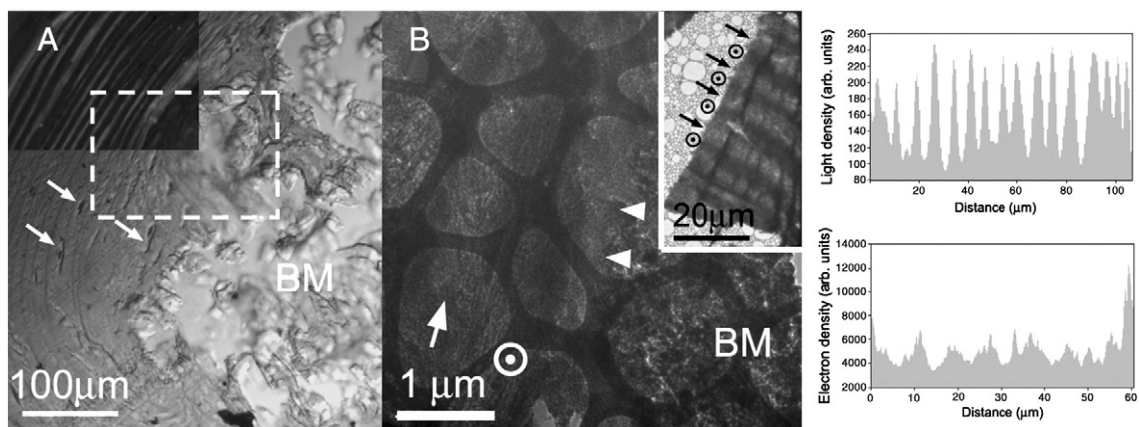

Fig. 3. Light microscopy and TEM images of regenerated bone surrounding the biomaterials (BM). (A) Differential interference contrast microscopy of regenerated bone (left side) surrounding HA-Alg biomaterial (BM). Arrows show osteocytes between bone lamellae. Inset: polarizing light microscopy image of the same region showing adjacent lamellae with collagen molecules in alternate orientations. Dashed rectangle indicates the region selected for observation in (B). (B) HA-Alg biomaterial (BM) surrounded by alternating bright (less electron-dense) and dark (more electron-dense) layers (lamellae), which correspond to regions with mineralized collagen fibrils approximately on the image plane (arrow) and fibrils approximately perpendicular to the image plane (circle), respectively. Arrowheads show the interface between biomaterial and bone. The dark network over the sections corresponds to the lacey carbon film texture. The inset shows a TEM image from the HA-Sint sample. The alternating electron density (arrows and circles) corresponds to the orientation of type I collagen in the lamellae. The image profiles show the light and electron intensity variations from adjacent lamellae obtained with the polarizing light microscope (Fig. 3A, inset) and TEM image (Fig. 3B, inset), respectively.

Regenerated bone after 90 days

New bone formed surrounding HA-Alg (Figs. 3A, B, Light Density Profile) and HA-Sint (Fig. 3B inset, Electron Density Profile) biomaterials presented a lamellar structure composed of concentric layers of collagen with alternating orientations. The region indicated by a dashed rectangle in Fig. 3A was prepared for further analyses by TEM and HRTEM. Because the lamellar structure, organization of the plate-like crystals and the sizes of apatite crystals (Table 1) were similar in both groups (HA-Alg and HA-Sint), we mainly present images obtained for the HA-Alg biomaterial. Using TEM, we observed the alternating concentric lamellae as high and low electron-dense layers corresponding to mineralized collagen fibrils in two different orientations (Fig. 3B). In both HA-Alg (Fig. 3B) and HA-Sint (Fig. 3B, inset) samples, the characteristic banding pattern of collagen was observed during analysis of the low electron-dense layers, indicating that the long axis of the molecules was oriented approximately in the plane of the section (Fig. 4A). SAED of the low electron-dense layer presented dispersion of the (002) hydroxyapatite ring (~60°), confirming a predominant orientation of apatite crystals along the type I collagen longer axes similar to bone (Fig. 4A, inset). Apatite crystals

in the low electron-dense layers were plate-like and were observed both side-on (dark lines — arrow) and top-on (less electron-dense with scarcely defined contours — arrowhead) (Fig. 4B).

Fig. 4C shows individual apatite nanocrystals from the same region. Crystals "a" and "b" were observed in the [210] and [100] zone axes, respectively. FFT of the HRTEM images showed that the [002] direction of both crystals, which corresponds to the length

Table 1
Hydroxyapatite crystals were measured using bright-field TEM from HA-Alg, HA-Sint and control samples (pre-existing cortical bone from rat calvaria). Length, width and thickness measurements were obtained in regions containing collagen-banding patterns with crystals predominantly oriented with the *c*-axis in the plane of the image. Width and thickness measurements were also obtained in transversal sections with crystals predominantly oriented with the *c*-axis perpendicular to image plane.

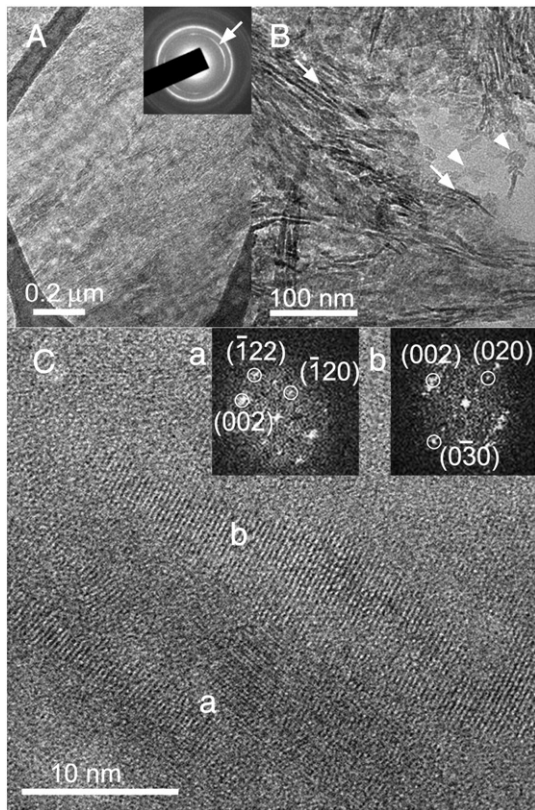|	Bone crystal (nm)			n
	Length	Width	Thickness	
HA-Alg	53.4 ($\pm$13)	20.0 ($\pm$7)	4.7 ($\pm$1)	60
HA-Sint	45.0 ($\pm$8)	16.5 ($\pm$4)	4.6 ($\pm$1)	60
Control	55.9 ($\pm$13)	18.9 ($\pm$6)	4.5 ($\pm$1)	60

Fig. 4. TEM of regenerated bone surrounding HA-Alg biomaterial. Bright (less electron-dense) layer containing collagen fibrils in the plane of the image. (A) Characteristic banding pattern of mineralized type I collagen fibrils. Inset: SAED of the banding pattern. The incomplete ring (arrow) corresponds to the (002) plane of hydroxyapatite, which is approximately parallel to the longer axis of the collagen. The external ring corresponds to 0.28 nm. (B) Nanocrystals associated with collagen were visible both side-on (arrow) and top-on (arrow read). (C) HRTEM of hydroxyapatite crystals. Crystals (a) and (b) were indexed in the [210] and [100] zone axes, respectively. Inset: FFT of lattice planes in crystals (a) and (b). Planes (002) point in the same direction within both crystals; however, the crystals are rotated by 19° around the c-axis.

circular patterns (Fig. 5A, dashed circles). SAED from these regions consistently showed continuous rings and the absence of (002) reflections (Fig. 5A, inset). The region indicated by an arrowhead in Fig. 5A was analyzed by HRTEM. Groups of plate-like nanocrystals observed end-on (in this case ~[002] direction) were frequently found to be rotated around a central region weakly crystalline or non-crystalline of about 30 nm in diameter (Figs. 5A and B). Arrows indicate the plate-like crystals from where thickness (t) and width (w) can be evaluated (Fig. 5B). A FFT from Fig. 5B showed the presence of (211) planes (arrow: 0.28 nm).

The size of the nanocrystals was measured using bright-field TEM in the two approximately orthogonal directions (longitudinal and transversal to collagen fibrils) from HA-Alg and HA-Sint samples and pre-existing calvaria rat bone (Table 1). The dimensions (length/width/thickness − nm) of bone crystals did not differ significantly between HA-Alg (53.4/20.0/4.7), HA-Sint (45.0/16.5/4.6) and pre-existing bone (55.9/18.9/4.5).

Small, round and electron-dense nanoparticles of 2.4 ($\pm$0.6) nm in diameter (n = 73) were observed adjacent to collagen fibrils, in a newly mineralized region where bone mineral density was still low, by HRTEM (Fig. 6A). The nanoparticles were crystalline (Fig. 6B) and frequently more electrondense than the surroundings (Fig. 6A). The interplanar distances measured in the Fig. 6B were 0.21 nm and 0.19 nm.

Cement layer

Fig. 7A shows an HRTEM image of the interface between HA-Alg particles (left side) and the newly formed tissue. The arrow in Fig. 7A points to a nanocrystal formed near the biomaterials particle. Many small weakly crystalline randomly oriented newly formed nanoparticles are also seen (Fig. 7A). FFT of the HRTEM image (Fig. 7A, inset) revealed the presence of (−12−2), (002) and (1−2−2) planes ([210] zone axis). A filtered image selecting the reflections indicated in the figure is also presented (Fig. 7A, inset).

At the same length scale, a similar ultrastructure was observed close to the HA-Sint biomaterial. Fig. 7B showed an HRTEM image of the biomaterial particle (left side) and newly formed apatite crystals (right side). The more electron-dense apatite crystal (Fig. 7B, arrow) is observed along the c-axis. FFT of this region exhibited a hexagonal pattern composed by (−130), (210), (3−20) lattice planes. Applying a hexagonal mask over the FFT spots enhanced the hexagonal lattice (Fig. 7B, inset).
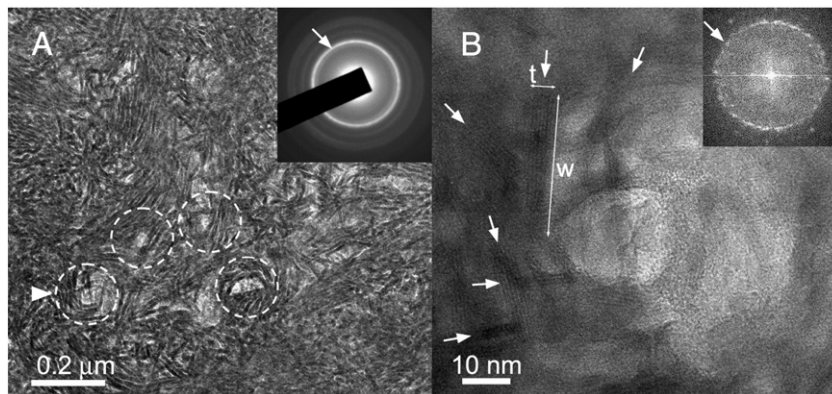
direction of the plate-like crystals, were oriented almost in parallel and that the crystals were rotated 19° around the c-axis relative to the other.

In the electron-dense layers, where collagen fibrils were oriented almost parallel to the EM beam, plate-like crystals formed arch or

Fig. 5. TEM of regenerated bone surrounding HA-Alg biomaterial. Lamella containing transversal sections of mineralized collagen fibrils. (A) Plate-like shaped hydroxyapatite crystals observed end-on; in some areas, the crystals are arranged in a circular pattern (dashed circles). The arrowhead indicates the region observed in (B). Inset: SAED showing a complete ring corresponding to (211) lattice planes (arrow). (B) HRTEM of the region indicated by the arrowhead in (A). Arrows indicate plate-like nanocrystals. Double headed arrows indicate width (w) and thickness (t) from nanocrystals. Inset: FFT from the image shows (211) planes (0.28 nm).
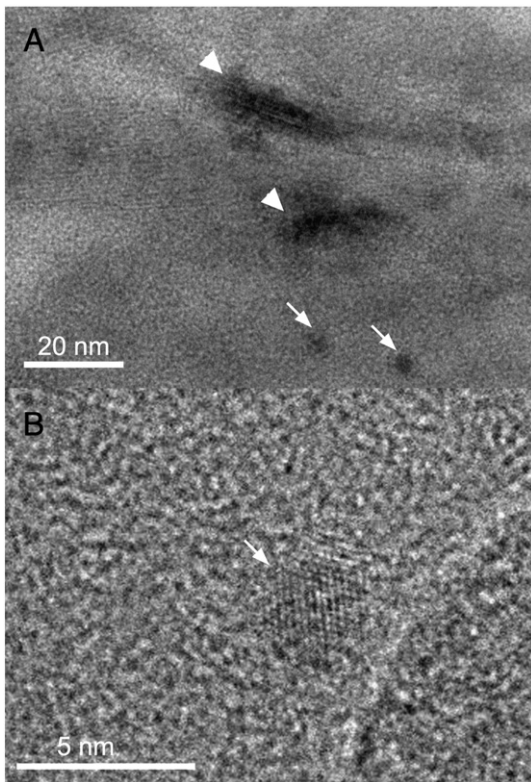
Fig. 6. Collagen fibrils from a weakly mineralized region and small electron-dense associated round particles. (A) Nanometer-sized round particles (arrow) were observed next to newly mineralized collagen fibrils (arrowheads). (B) HRTEM image showing that the round particles have a diameter of circa 3 nm and are crystalline (arrow). The distances between lattice planes measured directly in the figure were 0.21 nm and 0.19 nm.

Distinct mineralized layer

A distinct mineralized layer (DML) was often observed around HA-Alg and absent in HA-Sint samples. As shown in Fig. 8A, a DML was observed (circa 1 μm thick) in the vicinity of the HA-Alg sphere. Dark-field TEM from Fig. 8B demonstrated that this layer is composed of nanocrystallites (Fig. 8C). SAED of the DML exhibited continuous rings corresponding to 0.28 nm and 0.34 nm, indicating no preferential orientation of crystals (Fig. 8E).

The DML did not contain alternating lamellae as observed previously (Figs. 3A and B) or a characteristic banding pattern of collagen (Fig. 8B). The crystallites had a polyhedral morphology, which was different from that of bone crystals. The texture of this mineralized layer was also different; almost parallel fracture lines caused by sectioning with the diamond knife were always observed along the extension of this region in the section (Figs. 8A–C). The region inside the dashed square in Fig. 8B was analyzed by HRTEM. Fig. 8D shows a crystallite in the [001] zone axis. FFT of the lattice image exhibited a hexagonal pattern formed by planes of the kind (−110), (010) and (100) with 0.8 nm in distance (Fig. 8D, inset). Different from bone plate-like apatite crystals observed in the [001] zone axis, which are limited in thickness, the polygonal crystals from this mineralized layer had a symmetrical shape indicated by dashed lines in Fig. 8D.

As shown in Figs. 8E, F and G, we compared the SAED patterns obtained from three regions related to the HA-Alg biomaterial. The only continuous ring was seen in the DML (Fig. 8E). When a region closer to the interface between the DML and bulk region was analyzed, we observed a superposition of a pattern similar to the previous case with sharp spots, indicating the presence of larger nanoparticles from the biomaterial (Fig. 8F). When the selected area aperture was moved to the bulk of the biomaterial, we predominantly
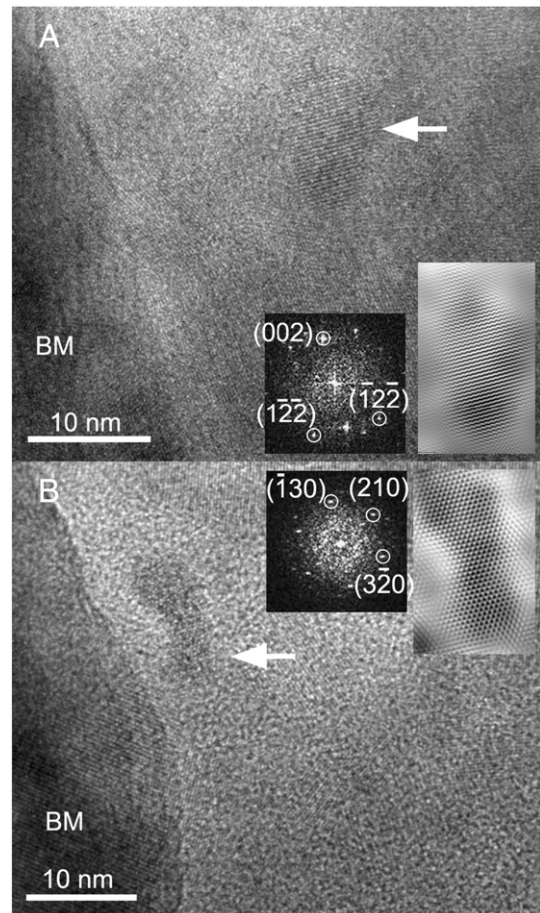

Fig. 7. HRTEM of the region close to the biomaterial. (A) HA-Alg biomaterial (BM) and mineralized regions (right size). Arrow indicates a hydroxyapatite crystal in the [210] zone axis. Inset: FFT of the crystal indicated by the arrow. The image of the crystal was reconstructed by applying a mask in the FFT image and selecting the (−12−2), (002) and (1–2–2) planes. (B) HA-Sint biomaterial (BM) and mineralized regions (right size). Arrow indicates a crystallite with a round contour indexed in the [001] zone axis of hydroxyapatite. Inset: FFT of the crystal indicated by arrow. Hexagonal pattern composed by the {210} family of planes. The image of the crystal was reconstructed by filtering the {210} planes in the FFT image.

saw sharp individual spots (Fig. 8G). All of these diffraction patterns were obtained under the same experimental conditions.

A nanocrystal from the bulk region of the biomaterial was analyzed by HRTEM (Fig. 9). The FFT image of the crystal is shown in inset. The symmetry of the lattice planes indicated that the crystal orientation was near the apatite [001] zone axis. The crystal exhibited geometrical contours (Fig. 9).

The sizes of the crystals from pre-existing bone (control — longitudinal section), the DML (after 90 days), and the bulk region of HA-Alg biomaterial after 90 days of implantation were measured from dark-field images (Table 2). The size of the biomaterial crystals was greater than the size of crystals in the DML and pre-existing bone. Although the shape of crystals in pre-existing bone was different from those of the DML, their sizes were similar when measured in dark field images (Table 2).

FTIR

Fig. 10A shows a band shift from 1028 cm^{-1} to 1013 cm^{-1} in both biomaterials (HA-Alg and HA-Sint) 120 days after implantation in comparison to intact biomaterials, suggesting that the apatite phase became less stoichiometric. Bands at 1086 cm^{-1} and 960 cm^{-1} did not move after implantation. We observed a broadening of the 1086 cm^{-1} and 960 cm^{-1} bands in the HA-Alg samples relative to
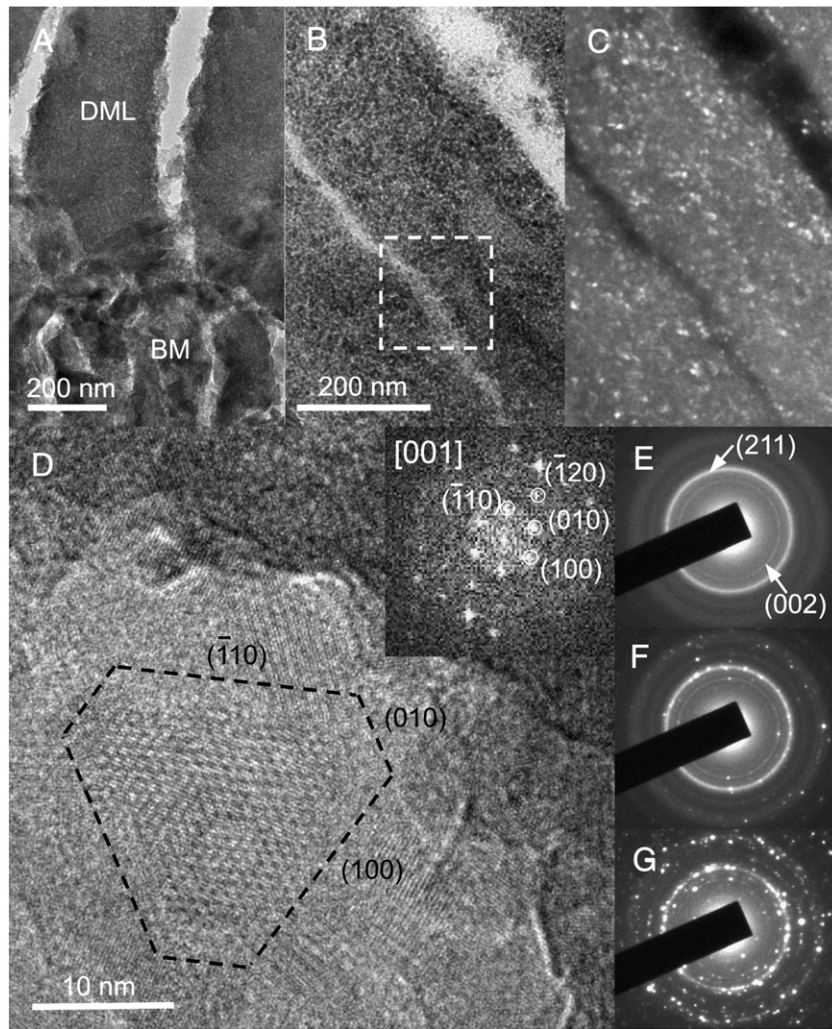
Fig. 8. TEM of the distinct mineralized layer (DML) surrounding the HA-Alg biomaterial. (A) Region containing the interface between a DML and the HA-Alg biomaterial (BM). (B) Bright field image of the DML The dashed square indicates the regions observed by HRTEM in (D). (C) Dark field image of (B). (D) HRTEM of the DML, showing a polyhedral hydroxyapatite crystal oriented in the *c*-axis. Dashed lines shows (−110), (010) and (100) planes. Inset: FFT of the polyhedral crystal showing spots from the [001] zone axis. (E), (F) and (G): SAED of DML (E), interface between the DML and biomaterial (F) and biomaterial (G). The same diffraction aperture and camera length were used. The arrow in (E) indicates the two most intense rings of the (002) and (211) planes (0.34 nm and 0.28 nm, respectively).

HA-Sint samples (Fig. 10B), indicating a more disordered apatite in HA-Alg sample after 120 days implantation. HA-Alg and HA-Sint biomaterials from different spheres are included in Fig. 10B.
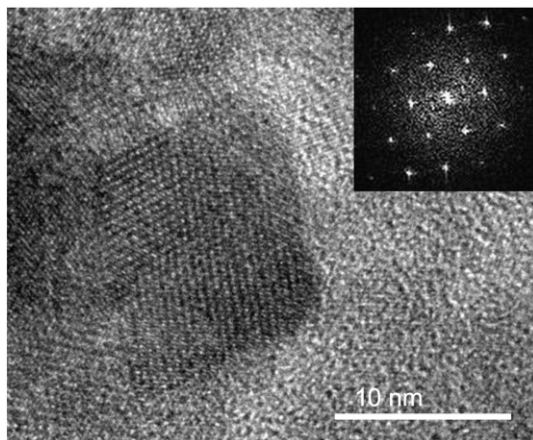

Fig. 9. HRTEM of HA-Alg grain approximately in the [001] zone axis. The crystal exhibits straight faces at an angle of approximately 120°, which is typical of synthetic hydroxyapatite crystals.

Discussion

A wide range of materials have been produced for bone engineering applications. As a consequence, specific biological/biomaterials responses are expected after implantation in bone tissue environment. The knowledge of the biomineralization and precipitation/reprecipitation process surrounding the biomaterials is of great importance to clinical applications.

In this work, we analyzed the ultrastructure of the new bone tissue formed around two distinct materials used as grafts: the composite HA-Alg and HA-Sint, which is obtained after calcination of the previous material. Our results indicated differences in the region

Table 2
In this table, the length of the hydroxyapatite crystals measured from collagen fibers in the control sample (pre-existing cortical bone from rat calvaria), is compared with the diameters of the crystals from DML and HA-Alg biomaterial, using dark-field TEM.

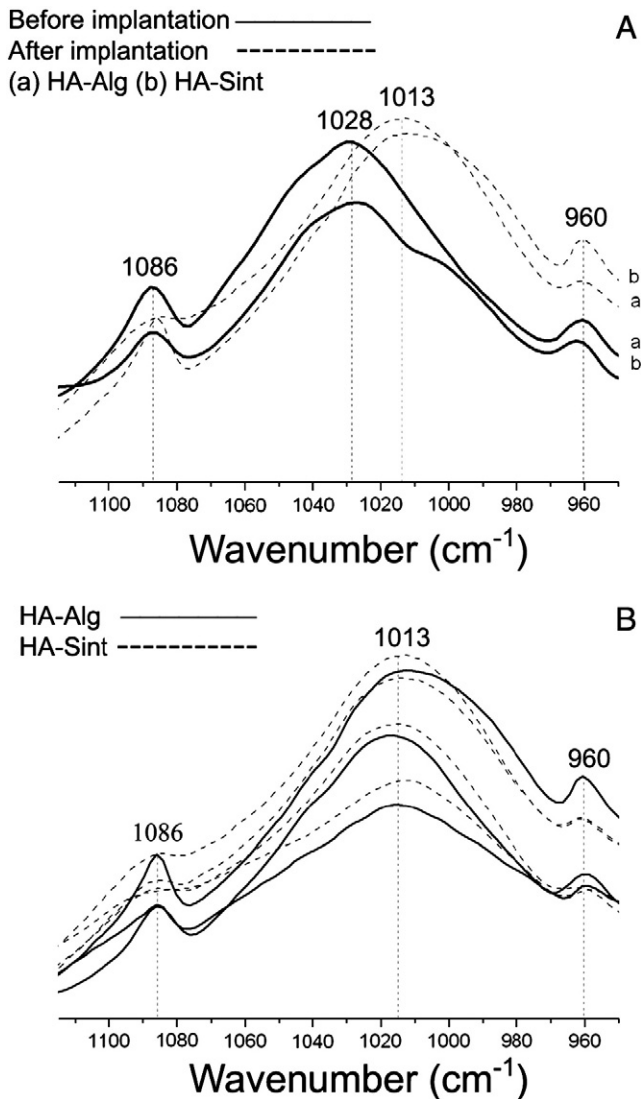|	Crystal size (nm)	n
Control	17.9 (±5)	20
DML	13.9 (±5)	20
HA-Alg biomaterial	81.5 (±32)	20

Fig. 10. FTIR of biomaterials. (A) Evolution of v_3PO_4 bands of HA-Alg (a) and HA-Sint (b) before (continuous line) and after (dot line) 120 days of implantation. After 120 days of implantation, the 1028 cm^{-1} band shifted to 1013 cm^{-1}, whereas the 1086 cm^{-1} and 960 cm^{-1} bands did not move. (B) v_3PO_4 bands of HA-Sint (continuous line) and HA-Alg (dot line) after 120 days of implantation (n=3 for both samples). HA-Alg samples presented broadening of the band at 1086 cm^{-1} when compared to HA-Sint samples, indicating a loss of crystallinity in HA-Alg relative to HA-Sint.

near the surface of HA-Alg when compared to HA-Sint. This zone is of particular interest because of the attachment of type I collagen fibrils and the consequent stability of the regenerated bone during the healing process.

Bone is a hierarchically structured composite formed by inorganic crystals embedded in an organic matrix composed mainly of type I collagen. The bone arrangement and interactions between the organic and inorganic constituents in different levels of organization contribute to diverse mechanical features and biological functions [14–17,27]. New mineralized tissue surrounding non-disaggregated or partially disaggregated HA-Alg and HA-Sint spheres after 90 days of implantation in the defects of rat calvaria was organized as micrometer-sized (1–5 μm) successive concentric lamellae. Each lamella contained roughly parallel type I collagen mineralized fibrils oriented in a specific direction. This type of arrangement is referred to as plywood where mineralized fibrils are arranged in discrete layers with the fibrils orientations in each layer being different from its neighbor [16,19].

It is generally accepted that woven bone is the first bone formed during initial bone formation in fracture and pathologic circumstances. Its rate of mineralization is faster than that of lamellar bone, resulting in the formation of smaller apatite crystals [21]. Bone formed directly in contact with the substrates (biomaterials) after 90 days presented a lamellar structure apparently without a previous woven bone stage. In contrast, bone formed inside critical defects near the remaining bone in the control group had a woven bone structure after the same period. The presence of a bioactive biomaterial (HA-Alg and HA-Sint spheres) together with the limitation of the volume of the defect allowed for the formation of structured bone.

Successive layers around HA-Alg and HA-Sint biomaterials were ultrathin sectioned transversally for further analysis by HRTEM. The resulting sections presented adjacent layers with fibrils in two orientations. This approach was used previously to describe the ultrastructure of the trabecular bone [30]. The fibrils orientation of each layer was deduced by crystals morphology (side, top and end-face-view) and SAED. In the same lamella, the c-axis of plate-like apatite crystals was aligned with adjacent crystals and with the long axis of collagen fibrils. However, crystals in the same layer were not organized in register. In fact, several crystals were rotated around the c-axis. This organization pattern was observed in transversal sections (electron-dense layer) by direct observation of the plate-like crystals end-on (Fig. 5). This nanometer level of organization was previously referred to as transversely isotropic [16], which is different from orthotropic symmetry when crystals are aligned in all three dimensional directions forming an extended crystalline structure as observed in mineralized turkey tendon [31].

Two sites of crystal nucleation, intra- or extra-fibrillar, have been reported for different bone types [26,28]. Intra-fibrillar mineralization was described for lamellar bone while extra-fibrillar mineralization was described in the early stage of tendon mineralization, in woven bone and in osteoblast cell culture mineralization [1,21,26]. Both mechanisms may take place together [21]. However, the association between organic and inorganic components is not always clear, and TEM observations occasionally result in controversial interpretations. The cross-section transmission electron micrographs of mineralized collagen where needle-like apatite crystals were observed surrounding less electron-dense circular regions observed in the present work (electron dense layer; Fig. 5) have also been observed by others [21,30]. The amorphous circular space surrounded by plate-like apatite crystals was associated with the non-mineralized intra-fibrillar space [21]. On the other hand, a similar cross-section pattern observed in trabecular bone was described as inter-fibrillar mineralization [30]. In the latter hypotheses, it was suggested that adjacent mineralized fibrils presented a specific angle of rotation around their long axes, which could explain the circular pattern produced by adjacent crystals. TEM analysis obtained in this work revealed that the circular regions (Fig. 5) had a diameter compatible to that of type I collagen fibrils (Fig. 4A). However, it cannot be discarded the possibility that parallel adjacent bone plate-like crystals correspond to intra-crystalline regions of collagen fibrils as the nanocrystals have constant distances between them, resembling other situations previously described [31]. Thus in these regions, circular patterns would be associated with the inter-fibrillar space.

Bone apatite crystals are plate-like shaped and have hexagonal symmetry. The average length, width and thickness of mature bone crystals were reported as $50 \times 25 \times 4$ nm [16], although a great range of values can be found in the literature [21,28,30,32]. The size of crystals in mature bone is greater than that in woven bone due to the high rate of absorption and new bone formation in woven bone [21]. In the present work, the dimensions of the new bone crystals formed surrounding HA-Alg biomaterial were 53.4 nm (length), 20.0 nm (width), 4.4 nm (thickness) (end-on, side-on views, Table 1), in agreement with literature values for mature bone.

Measurements on crystallite dimensions are difficult to obtain. Although side-on and end-on views show needle-like crystals in high contrast, these observations may correspond to the superposition of other nanocrystals through the section. On the other hand, top-on views of thin crystals are not accurate because of the low contrast of the image. Measurements obtained with dark-field microscopy are more accurate and can even show that "individual crystals" of bone may be polycrystalline. As a general rule, we should consider that measurements with bright field give larger dimensions than those with dark field. In the present work, we conducted measurements to compare, by the same approach, the newly formed crystals with those in the original bone. Our results showed that regenerated bone formed around the biomaterials and preexisting bone had similar dimensions.

Small round particles of approximately 3 nm were observed close to collagen fibrils in the initial stage of mineralization. Similar particles were previously observed in trabecular bone [33] and have been associated with the initial stages of mineralization in zebra fish fin bones [34] and chicken bones [35]. Mahamid et al. [34] described particles ranging from 10 to 15 nm by high-resolution SEM while Hong et al. [33] reported particles measuring approximately 2 nm based on HRTEM. These authors suggested that these particles are responsible for the formation of hydroxyapatite crystals associated with the fibrils. Cuisinier et al. [35] proposed a hypothesis in which plate-like apatite crystals are composed of many nanoparticles fused together. The nucleation and growth direction of neighboring nanoparticles should be governed by the same organic substrate, resulting in partial alignment between particles that compose a plate-like apatite crystal. Thus, even the hydroxyapatite "nanoparticles" of bone are polycrystalline, an example of non-classical mineralization (nucleation in multiple sites and further alignment due to proteins [36]). Slight misorientations between nanoparticles were observed by Cuisinier et al. [35] and are in agreement with the fact that plate apatite crystals are not monocrystals [33,34] (this work). The resulting plate-like crystals would present boundaries between grains, which is the result of the independent nucleation site, growth and subsequent fusion. The last stage of plate-like crystal formation is the fusion of lateral faces and is accomplished through high-angle grain boundaries [35].

The adjacent crystals shown in Fig. 4C presented lateral close apposition in which crystals were turned by about 19° around the c-axis, while the [001] directions were oriented approximately in parallel. The chemical interaction between apatite crystals nuclei and the organic matrix substratum which determines the crystal orientation shows that the whole composite presents a more specific alignment along the c-axis (the longer axes of the fibrils) and can rotate to some extent around the axes.

The cement layer-like region was analyzed in HA-Alg and HA-Sint biomaterials. No collagen molecules were observed in this layer and apatite nanocrystals in both HA-Alg and HA-Sint samples presented an elongated shape with no preferential orientation. No evidence of epitaxial growth was observed in the surface of the biomaterial in our work although this type of crystal growth had been suggested before [9]. Our result may suggest that even those regions in close contact with the biomaterial are under strong biological control.

Although high-resolution imaging in TEM is of particular interest to determine the micro/nanostructure of bone mineral [21,30] and the interface of new bone and biomaterials [2,9] only a small part of the specimen is observed. To overcome this limitation a high number of specimens were observed previously [13] by light microscopy (bright field, differential interference contrast and polarizing light modes) and conventional transmission electron microscopy to better sampling and determine the regions of interest.

Some differences were noted in the regenerated bone surrounding HA-Alg relatively to HA-Sint spheres, after 90 days. In a submicrometer scale we observed a distinct mineralized layer (DML) in the interface between new bone and HA-Alg. This zone contained crystals with specific morphologies (Fig. 8) that differentiates it from pre-existing and regenerated bone, the cement layer and the bulk of the biomaterial. The absence of the DML in the contour of the HA-Sint biomaterial suggests that the formation of this layer is related to the presence of alginate phase to some extent.

Dissolution of calcium phosphate from the hydroxyapatite biomaterial is reported to enhance bone mineral formation by local increase of ions [37]. Thus a dissolution–reprecipitation mechanism involving synthetic HA-Alg crystals along the healing process could explain the mineralization of hydroxyapatite in the DML region. Another hypothesis would involve the interaction between the synthetic nanoparticles and alginate. Hydroxyapatite crystals mixed with sodium alginate form a non-homogeneous composite, due to the dispersion on the distribution of particles diameters. When the assemblage is dropped in a $CaCl_2$ solution, the alginate phase is polymerized forming the known egg-box structures and would encapsulate the smaller particles more evenly inside the network just formed, while the larger ones would be dispersed far apart.

The calcination process for the formation of HA-Sint biomaterial produced a more homogeneous material eliminating any pre-existing amorphous phases and minimizing morphological inhomogenities, producing a final biomaterial with a highly mineralized surface, different from HA-Alg. This feature could contribute to the different behavior of the biomaterials in the interface with new bone formed, reinforcing the importance of studying this specific region in the context of bone engineering.

Conclusion

The newly formed bone surrounding both biomaterials presented a lamellar structure, showing that the biomaterials facilitated a quick approach to produce structured bone. The main structural differences were found in the vicinity of the biomaterials (cement layer-like region) where the HA-Alg sample was surrounded in a large extent by a DML, indicating that this material had/induced a more diverse ultrastructure than HA-Sint. No evidence of epitaxial growth was observed in any of the materials, indicating that there is a biological control on homeostasis to some degree, even in this region. FTIR showed that both biomaterials changed in vivo after implantation being less structured when compared with the original samples. This fact was more pronounced in HA-Alg sample, showing again that this biomaterial presented a higher change when compared with the sintered sample. These results indicate that the diverse substructures found at different length scales, particularly at the nanoscale, may be used to indicate specific biological/biomaterials response after implantation.

This study showed that round nanoparticles recently described in trabecular bone [33] and growing fin bones of the zebra fish [34] are also present in initial stages of bone mineralization surrounding a biomaterial in a critical defect. This finding reinforces the hypothesis that newly formed bone is correlated with the presence of round nanoparticles, which would be associated with nucleating events.

References

[1] Davies JE. In vitro modeling of the bone/implant interface. Anat Rec 1996;245: 426–45.
[2] Davies JE, Baldan N. Scanning electron microscopy of the bone–bioactive implant interface. J Biomed Mater Res 1997;36:429–40.

[3] Anselme K. Osteoblast adhesion on biomaterials. Biomaterials 2000;21:667–81.
[4] Rodrigues CVM, Serricella P, Linhares ABR, Guerdes RM, Borojevic R, Rossi MA, et al. Characterization of a bovine collagen-hydroxyapatite composite scaffold for bone tissue engineering. Biomaterials 2003;24:4987–97.
[5] Thian ES, Loh NH, Khor KA, Tor SB. Microstructures and mechanical properties of powder injection molded Ti-6Al-4V/HA powder. Biomaterials 2002;23:2927–38.
[6] Ribeiro CC, Barrias CC, Barbosa MA. Calcium phosphate–alginate microspheres as enzyme delivery matrices. Biomaterials 2004;25:4363–73.
[7] Neumann M, Epple M. Composites of calcium phosphate and polymers as bone substitution materials. Eur J Trauma 2006;32:125–31.
[8] Izquierdo-Barba I, Colilla M, Vallet-Regí M. Nanostructured mesoporous silicas for bone tissue regeneration. J Nanomater 2008;2008:1–14.
[9] Hemmerlé J, Cuisinier FJG, Schultz P, Voegel JC. HRTEM study of biological crystal growth mechanisms in the vicinity of implanted synthetic hydroxyapatite crystals. J Dent Res 1997;76:682–7.
[10] Bernhardt A, Despang F, Lode A, Demmler A, Hanke T, Gelinsky M. Proliferation and osteogenic differentiation of human bone marrow stromal cells on alginate–gelatine–hydroxyapatite scaffolds with anisotropic pore structure. J Tissue Eng Regen Med 2009;3:54–62.
[11] Lin HR, Yeh YJ. Porous alginate/hydroxyapatite composite scaffolds for bone tissue engineering: preparation, characterization, and in vitro studies. J Biomed Mater Res B 2004;71B:52–65.
[12] Parhi P, Ramanan A, Ray AR. Preparation and characterization of alginate and hydroxyapatite-based biocomposite. J Appl Polymsci 2006;102:5162–5.
[13] De Paula F, Barreto I, Rocha-Leão M, Borojevic R, Rossi A, Rosa F, et al. Hydroxyapatite–alginate biocomposite promotes bone mineralization in different length scales *in vivo*. Front Mater Sci China 2009;3:145–53.
[14] Rho JY, Kuhn-Spearing L, Zioupos P. Mechanical properties and the hierarchical structure of bone. Med Eng Phys 1998;20:92–102.
[15] Mann S. Biomineralization principles and concepts in bioinorganic materials chemistry. New York: Oxford University Press; 2001.
[16] Weiner S, Wagner HD. The material bone: structure–mechanical function relations. Annu Rev Mater Sci 1998;28:271–98.
[17] Weiner S, Traub W, Wagner HD. Lamellar bone: structure–function relations. J Struct Biol 1999;126:241–55.
[18] Ziv V, Wagner HD, Weiner S. Microstructure–microhardness relations in parallel-fibered and lamellar bone. Bone 1996;18:417–28.
[19] Giraud-Guille MM, Besseau L, Martin R. Liquid crystalline assemblies of collagen in bone and in vitro systems. J Biomech 2003;36:1571–9.
[20] Weiner S, Arad T, Traub W. Crystal organization in rat bone lamellae. FEBS Lett 1991;285:49–54.
[21] Su X, Sun K, Cui FZ, Landis WJ. Organization of apatite crystals in human woven bone. Bone 2003;32:150–62.
[22] Zhou H, Chernecky R, Davies JE. Deposition of cement at reversal lines in rat femoral bone. J Bone Miner Res 1994;9:367–74.
[23] Ozawa H, Hoshi K, Amizuka N. Current concepts of bone biomineralization. J Oral Biosci 2008;50:1–14.
[24] Yang L, Zhang Y, Cui FZ. Two types of mineral-related matrix vesicles in the bone mineralization of zebrafish. Biomed Mater 2007;2:21–5.
[25] Bonucci E. Crystal ghosts and biological mineralization: fancy spectres in an old castle, or neglected structures worthy of belief? J Bone Miner Metab 2002;20:249–65.
[26] Landis WJ, Hodgens KJ. Mineralization of collagen may occur on fibril surfaces: evidence from conventional and high-voltage electron microscopy and three-dimensional imaging. J Struct Biol 1996;117:24–35.
[27] Landis WJ, Silver FH. The structure and function of normally mineralizing avian tendons. Comp Biochem Phys A 2002;133:1135–57.
[28] Landis WJ, Song MJ, Leith A, McEwen L, McEwen BF. Mineral and organic matrix interaction in normally calcifying tendon visualized in three dimensions by high-voltage electron microscopic tomography and graphic image reconstruction. J Struct Biol 1993;110:39–54.
[29] Mavropoulos E, Rocha-Leão MH, Rocha NCC, Prado MH, Rossi AM. Hydroxyapatite–alginate composite for lead removal in artificial gastric fluid. J Mater Res 2007;22:3371–7.
[30] Rubin MA, Jasiuk I, Taylor J, Rubin J, Ganey T, Apkarian RP. TEM analysis of the nanostructure of normal and osteoporotic human trabecular bone. Bone 2003;33:270–82.
[31] Weiner S, Traub W. Organization of hydroxyapatite crystals within collagen fibrils. FEBS Lett 1986;206:262–6.
[32] Robinson RA. An electron-microscopic study of the crystalline inorganic component of bone and its relationship to the organic matrix. J Bone Joint Surg Am 1952;34:389–476.
[33] Hong S, Hong S, Kohn D. Nanostructural analysis of trabecular bone. J Mater Sci Mater Med 2009;20:1419–26.
[34] Mahamid J, Sharir A, Addadi L, Weiner S. Amorphous calcium phosphate is a major component of the forming fin bones of zebrafish: indications for an amorphous precursor phase. Proc Natl Acad Sci U S A 2008;105:12748–53.
[35] Cuisinier FJG, Steuer P, Brisson A, Voegel JC. High resolution electron microscopy study of crystal growth mechanisms in chicken bone composites. J Cryst Growth 1995;156:443–53.
[36] Niederberger M, Colfen H. Oriented attachment and mesocrystals: non-classical crystallization mechanisms based on nanoparticle assembly. Phys Chem Chem Phys 2006;8:3271–87.
[37] Ducheyne P, Qiu Q. Bioactive ceramics: the effect of surface reactivity on bone formation and bone cell function. Biomaterials 1999;20:2287–303.